DOI: 10.21062/mft.2026.015 http://www.journalmt.com

Influence of the Manufacturing Route on the High-Temperature Oxidation Behavior of IN718 Alloy in Simulated Modern Energy Environments

Patrícia Lovašiová (0000-0002-1969-6453)[1], Jan Hruška (0000-0003-4899-0536)[1], Tomáš Lovaši (0000-0002-3960-4261)[1], Miroslav Zetek (0000-0003-2599-2061)[2], Yusuf Bakir (0000-0002-4017-9522)[2], Ivana Zetková (0000-0003-2415-922X)[2]
[1]SVÚM a.s., Tovární 2053, 250 88 Čelákovice, Czech Republic. E-mail: lovasiova@svum.cz
[2]Faculty of Mechanical Engineering, University of West Bohemia, Univerzitní 2732/8, 301 00 Pilsen, Czech Republic

The use of supercritical water in energy applications is motivated by the aim of increasing the thermal efficiency of power systems. However, structural materials exposed to this environment may undergo corrosive degradation. The objective of this study was to conduct experiments on samples exposed to simulated operational conditions in supercritical water, steam, and air. The material surfaces were subsequently analyzed using optical microscopy and scanning electron microscopy coupled with energy-dispersive spectroscopy (SEM/EDS). Particular attention was given to the formation of oxide layers on the nickel-based alloy Inconel 718 produced by additive manufacturing by PBF-SLM technology. The corrosion behavior was evaluated by monitoring mass gains. The results were compared with materials manufactured using conventional techniques.

Keywords: Inconel 718 alloy, Supercritical Water, SCWR, Steam, Additive Manufacturing Technology

1 Introduction

With the growing demand for clean and affordable electricity, the pressure to develop advanced power generation technologies is also increasing. One of the promising directions is nuclear reactors IV. Generation, with particular attention given to the concept of the Supercritical Water Reactor (SCWR). This concept combines operational experience from both nuclear and conventional thermal power plants and offers higher thermodynamic efficiency while potentially reducing capital costs. The SCWR operates in a direct-cycle mode at a pressure of 25 MPa, with the coolant entering the core at 280 °C and exiting at temperatures of up to 620 °C. In the supercritical regime, no liquid–steam phase transition occurs, ensuring single-phase flow throughout the system. However, these extreme environments impose significant demands on structural materials. In particular, there must be no loss of mechanical properties such as ductility, strength, corrosion resistance, and resistance to stress corrosion cracking. These properties are strongly influenced by the abrupt change in the physicochemical characteristics of water when transitioning from the subcritical to the supercritical state. One of the key objectives in the development of fourth-generation nuclear reactors, introduced in 2001, is not only to improve efficiency but also to enhance safety and reduce the risk of nuclear technology proliferation. SCWRs employ inlet steam with supercritical parameters (T > 374 °C, p > 22.1 MPa), which enables efficiencies exceeding 45%. Under these conditions, current materials are inadequate, highlighting the necessity for the development of new, more suitable alloys [1,2,3,4,5].

In nuclear reactors that use water under supercritical conditions as the working medium, zirconium alloys commonly employed in subcritical units cannot be used for fuel cladding. Previous research has identified corrosion-resistant austenitic steels and nickel-based superalloys as potential alternatives. These materials exhibit varying degrees of suitability in terms of their physicochemical and mechanical properties, which require detailed characterization. Nickel-based superalloys are particularly applied in high-demand environments such as aerospace, astronautics, and nuclear power, owing to their excellent strength, toughness, and resistance to creep, corrosion, and oxidation at elevated temperatures. These properties are primarily attributed to their face-centered cubic (fcc) structure [3,5].

Nickel-based superalloys achieve their exceptional properties through a combination of solid-solution strengthening by alloying elements, precipitation of intermetallic phases, and carbide formation. Their matrix consists of group 10 elements of the periodic table (Ni, Fe, Co), often combined with Cr, Mo, Nb, Ta, Ti, and Al. Oxidation resistance is provided by the formation of protective Al_2O_3 and Cr_2O_3 layers[4,5].

One of the frequently used nickel-based superalloys is Inconel 718 – a precipitation-strengthened nickel-chromium-iron alloy with additions of niobium and molybdenum. The alloy exhibits high strength, creep resistance, excellent toughness, and corrosion stability up to 700 °C. These properties make it suitable for applications in SCWRs and other high-temperature systems, as well as for the construction of turbine blades [3,5,6].

Inconel 718 is strengthened by precipitation hardening through γ' ($Ni_3(Al,Ti)$) and γ" (Ni_3Nb) phases. Due to its high strength, fatigue resistance, and good corrosion resistance, it is widely used at elevated temperatures. Although the alloy exhibits excellent properties, its microstructure is sensitive to the formation of undesirable phases, such as δ, η, and particularly the Laves phase. These phases, which form during prolonged exposure at high temperatures or during welding, adversely affect mechanical properties, especially creep strength and fracture resistance. The Laves phase, which forms in the heat-affected zone, promotes crack initiation due to liquation and reduces the toughness of the weld. Therefore, special attention must be given to heat treatment, which influences the size and distribution of the precipitate phases, to achieve an optimal microstructure with uniformly dispersed γ' and γ" particles. A properly controlled process increases component service life and minimizes the risk of undesirable phase formation, which is critical for applications under demanding operating conditions, such as components in nuclear power systems [4,7,8,9].

In recent years, the use of additive manufacturing (AM) technologies for producing complex-shaped components has significantly expanded, not only for nickel-based superalloys. AM approaches, such as Selective Laser Melting (SLM), Electron Beam Melting (EBM), and Laser Metal Deposition (LMD), enable the production of components with minimal waste and high precision. Techniques such as SLM further allow processing a wide range of materials, including superalloys, and find applications in industries such as aerospace and power engineering. The use of AM technologies for manufacturing Inconel 718 components represents a promising direction, combining excellent material properties with geometric flexibility [8].

The aim of this study was to experimentally evaluate the general corrosion behavior and the characteristics of oxide layers formed on the nickel-based superalloy Inconel 718, produced by additive manufacturing, at an exposure temperature of 650 °C in different environments – supercritical water (SCW), saturated steam, and air – in order to simulate the operating conditions of advanced fourth-generation SCWRs (Supercritical Water Reactors) or steam turbine operation. Gravimetric methods were employed to quantitatively assess corrosion attack and determine corrosion rates. Subsequently, a detailed microstructural characterization of the formed oxide layers was performed to elucidate the oxidation mechanism and to identify differences in morphology and composition depending on the exposure environment.

2 Experimental procedure

2.1 Production and Preparation of Test Samples

The experimental material used in this study was the nickel-based alloy Inconel 718 (hereafter referred to as EOS718), produced by the SLM method using an EOS M290 3D printer (EOS, GmbH), which employs a ytterbium fiber laser with a maximum power of 400 W – see Fig. 1.

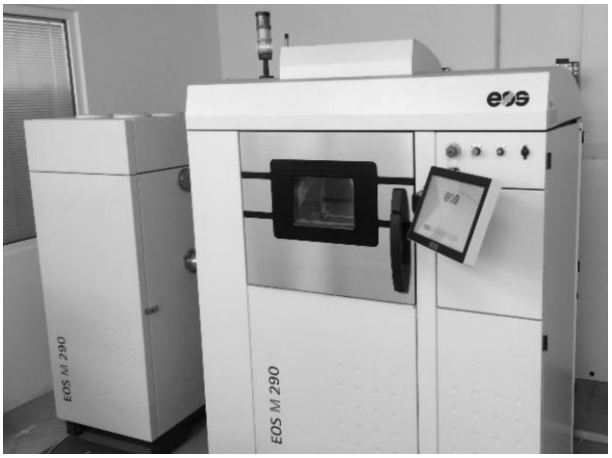

Fig. 1 *EOS M290 – 3D printer [10]*

A cast material in the as-cast condition (hereafter referred to as ALLOY718), purchased from an industrial supplier, was used as the reference material. Since these materials are conventionally employed after specific heat treatment and hardening, all tested samples were subjected to the same processing to allow for comparison with the conventional condition.

The heat treatment was performed according to [11]. A schematic representation is shown in Fig. 2. The samples were first heated to 1065 °C for one hour for solution annealing and were then slowly cooled in air or under an argon protective atmosphere. This was followed by a two-step aging process. The first step was conducted at 760 °C for 10 hours, after which the samples were cooled at a rate of 50 °C/h to 650 °C, where the second aging step was carried out for 8 hours. Upon completion of the required duration, the samples were again slowly cooled in air or under an argon protective atmosphere.

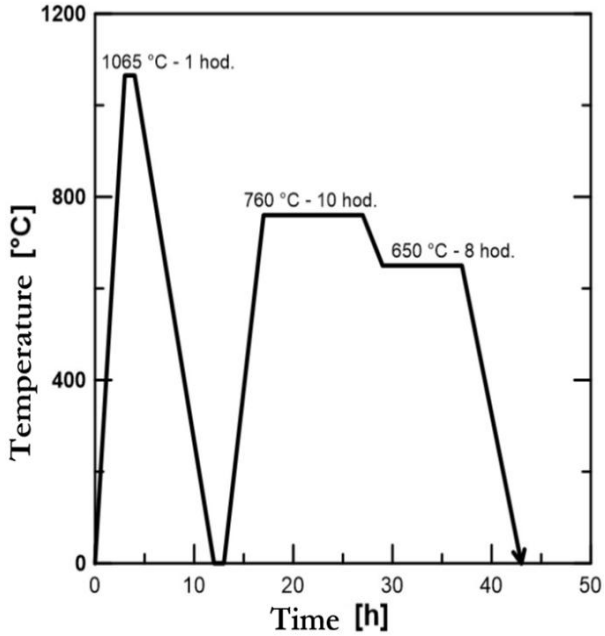

Fig. 2 *Schematic Representation of the Heat Treatment Process According to ASM 5664 [12]*

Samples for the exposure tests were cut from each material using an ATM Brillant 220 precision metallographic saw at laboratory temperature. They were then manually ground with abrasive papers and degreased. The samples were weighed, measured, and subsequently exposed in three environments simulating real operating conditions in power systems – air, steam at 650 °C (for 100, 200, 500, and 1000 hours), and supercritical water at 650 °C and 30 MPa for 500 and 1000 hours. For each combination of environment, material and exposure time, six samples were prepared.

2.2 Methodology for Exposures in Simulated Environments

2.2.1 Exposure in air and steam at a temperature of 650 °C

The samples were exposed to atmospheric air in an electrically heated chamber furnace with forced air circulation, ensuring uniform temperature distribution and a stable furnace atmosphere throughout the entire exposure period. Simultaneously, exposure in steam was conducted in a tube furnace with a metal muff. The model steam environment consisted of a mixture of air and water vapor, with air serving as the carrier gas to ensure a constant flow of the atmosphere within the furnace. Both types of furnaces are shown in Fig. 3. The exposures were carried out at 650 °C under atmospheric pressure for 1000 hours. After the exposure period, the samples were removed, cooled in air at room temperature, and weighed. They were then subjected to standard metallographic evaluation.

Fig. 3 *Chamber furnace with circulation and tube furnace with metal muff*

2.2.2 Exposure in Supercritical Water at 650 °C and 30 MPa

High-temperature corrosion tests were also performed to simulate operation in supercritical water at 650 °C and 30 MPa. The static autoclave used had a capacity of six individual samples (Fig. 4), placed in a separate corundum boat. Accordingly, three samples of IN718 alloy produced by conventional methods (ALLOY718) and three samples of IN718 alloy produced by 3D printing (EOS718) were exposed. The autoclave was then filled with demineralized water, pressurized to 30 MPa, and heated to 650 °C.

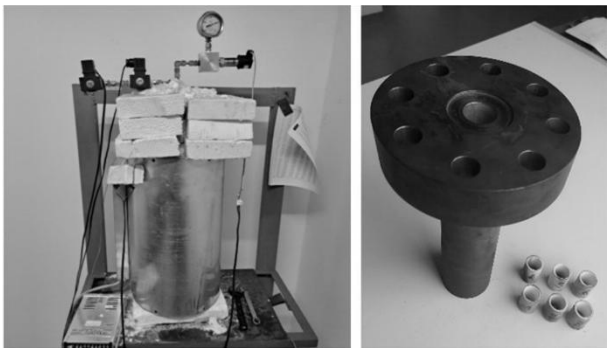

Fig. 4 *High-pressure autoclave and set of specimens in corundum crucibles*

2.3 Methodology for Evaluation of Samples after Exposure

The primary method for evaluating corrosion resistance after all types of exposure was the gravimetric method, which monitored changes in sample mass over time. The mass change due to corrosion, typically assessed using this method, is expressed as the mass change of the sample relative to its surface area. If corrosion products spall off or are removed by dissolution, the gravimetric method usually indicates a mass loss. Conversely, if corrosion products adhere firmly to the sample surface after exposure, this is reflected as a mass gain [3]. However, this method has its limitations and therefore had to be complemented with metallographic evaluation. The corrosion rate by the gravimetric method was calculated from the mass losses/gains of the given

material over a specific time. Weighing was performed using SARTORIUS MC1 AC 120S analytical balances with a resolution of 0.1 mg and a linearity of ≤±0.0002 g. For each experimental condition, six independent specimens were evaluated. The reported values represent arithmetic means, while the variability of the data is expressed by standard deviations shown as error bars in the corresponding graphs. Considering the analytical balance resolution of 0.1 mg and the linearity of ≤±0.0002 g, the instrumental uncertainty becomes significant when evaluating very small mass changes. In several cases, the measured values were close to the detection limit of the method. The relative uncertainty is therefore more pronounced at shorter exposure times, when oxide layers are still thin and mass changes minimal. With increasing exposure time, the signal-to-noise ratio improves as the oxide layer grows. These aspects were taken into account when interpreting the gravimetric data. In this study, repeated weighing was performed during exposure at 100, 200, 500, and 1000 hours. For autoclave exposure, weighing was carried out after 500 and 1000 hours.

The materials were subsequently subjected to standard metallographic evaluation to analyze the formed layers and degradation processes. The samples were then etched with Lindall's reagent for 2–5 seconds to enable more detailed observation of the microstructure, enhancing the visibility of particles and precipitates. The prepared cross-sections were examined using a Zeiss Axio Observer metallographic optical microscope. Elemental microanalysis and observation of the oxide layers were performed using a Zeiss EVO MA10 scanning electron microscope equipped with an EDS analyzer.

3 Results and discussion

3.1 Chemical Composition

The chemical composition of Inconel 718 was analyzed using optical emission spectroscopy with a spark excitation source (OES, Optical Emission Spectroscopy). The measurements were conducted to compare the conventionally manufactured material (Alloy718) with the specimen produced by additive manufacturing using the SLM method (EOS718).

The results of the chemical analysis are summarized in Tab. 1. The reported elemental concentrations are expressed in weight percent (wt.%). The values represent average contents from five individual measurements. Both analyzed variants of the alloy exhibit comparable chemical compositions consistent with the standard for Inconel 718 (e.g., AMS 5662 / ASTM B637), without significant deviations in elements such as Ni, Cr, Fe, Nb, or Mo. This confirms the material equivalence in terms of chemical composition between the conventionally produced and the additively manufactured material.

Tab. 1 *Chemical Composition of Materials*

	Ni	Cr	Fe	Nb	Mo	Ti	Al	Mn	C	S	Co
ALLOY718	50.66±0.05	19.17±0.01	20.37±0.06	4.46±0.05	3.22±0.01	0.89±0.01	0.47±0	0.10.±0	0.05±0	0.01±0	0.29±0.01
EOS718	51.04±0.11	19.96±0.09	19.55±0.04	4.42±0.04	3.26±0.02	0.96±0.02	0.48±0.02	0.05±0.01	0.06±0.01	0.01±0	0.03±0.01

The lower cobalt content in the powder alloy (EOS718) represents a significant advantage for nuclear energy applications, as it reduces the formation of radioactive ^{60}Co through neutron activation. This isotope is a strong gamma emitter and, even at trace concentrations, contributes significantly to the radiation exposure of personnel. For this reason, strict limits on the maximum allowable cobalt content in structural materials are applied in nuclear energy, particularly in areas exposed to neutron flux. Corrosion products containing ^{60}Co can contaminate the coolant and increase the radiation levels within the system [1,3,13].

3.2 Microstructure

The microstructure of conventionally processed and additively manufactured Inconel 718 alloy prior to exposure in each environment is summarized in Fig. 5. The microstructure of conventionally prepared Alloy718 after heat treatment exhibits equiaxed grains, primarily composed of the γ matrix (Ni-based solid solution). The individual grains are of homogeneous size and are clearly defined by etching, indicating effective recrystallization during heat treatment. Fine precipitates can be locally observed at the grain boundaries, which, based on their morphology and the known aging behavior of the alloy, can be attributed to the δ phase (Ni_3Nb). These precipitates are mainly located at the grain boundaries and, to a lesser extent, within the grains, where they contribute to microstructural stabilization by limiting grain growth [14,15].

Bright features corresponding to primary carbides (Fig. 6), particularly NbC with possible Ti and Mo additions, were further observed at the grain boundaries [15,16]. As carbon is not detected in EDS analysis, the phases were identified solely based on morphology, dominant elements, and literature references. In nickel-based alloys, carbon content is generally kept to a minimum, despite its potential beneficial effects. Carbon reacts with elements such as Mo, Ti, and Nb to form primary carbides, commonly designated as MC.

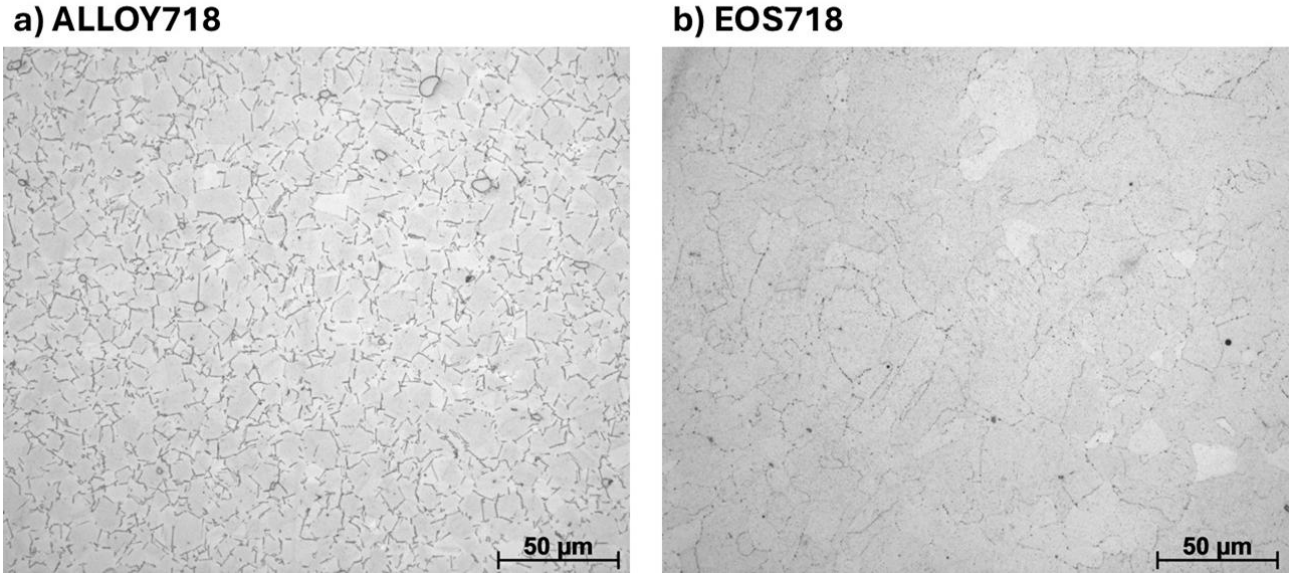

Fig. 5 *Microstructure of Samples before Exposure – Optical Microscope*

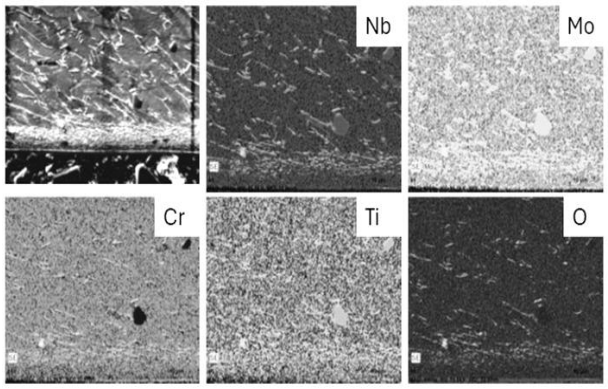

Fig. 6 *Elemental distribution map emphasis on carbide identification in the ALLOY718*

These carbides form during solidification of the alloy and persist even after heat treatment. The presence of carbides can have an ambivalent effect on the alloy´s properties – on one hand, they can stabilize the grain struc-ture and contribute to limiting plastic deformation; on the other hand, they can serve as potential initiation sites for damage under high-temperature loading, and if continuous carbide networks occupy the grain boundaries, the material loses its ductility. According to the literature [17,18,19], secondary carbides of the type $M_{23}C_6$, M_6C or M_7C_3 may also be present in the matrix. Increased concentrations of these elements were also detected by EDS analysis in the form of a line scan, shown in Fig. 7.

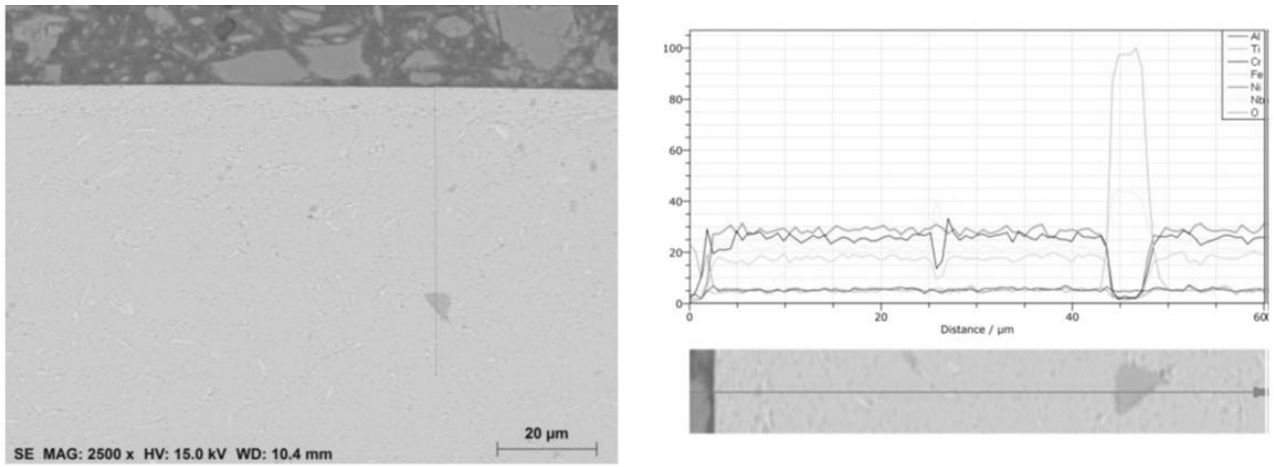

Fig. 7 *Line scan of the ALLOY718 specimen across a carbide particle*

In 3D-printed Inconel 718, the microstructure is highly dependent on the orientation of the observed plane. For a better understanding of the microstructure and orientation of the printed specimen, Fig. 8 shows a 3D view of the structure. The microstructure of Inconel 718 produced by SLM is distinctly different from conventionally processed material even under optical microscopy. After etching, a finely layered, lamellar texture is visible, reflecting the sequential deposition of individual layers during

the printing process. In specimens oriented in the X–Z and Y–Z directions, elongated grains can be observed along the solidification direction, exhibiting mostly random orientation and pronounced morphological inhomogeneity. This phenomenon is associated with the thermal effect of the laser, which penetrates into the underlying layers, causing partial melting and subsequent bonding of powder particles, leading to the formation of elongated grains. In the X–Y plane, corresponding to a single printed layer, a linear structure appears, formed by larger grains surrounded by a fine-grained matrix. This morphology is closely related to the trajectory and scanning strategy of the laser beam during the melting process [8,20].

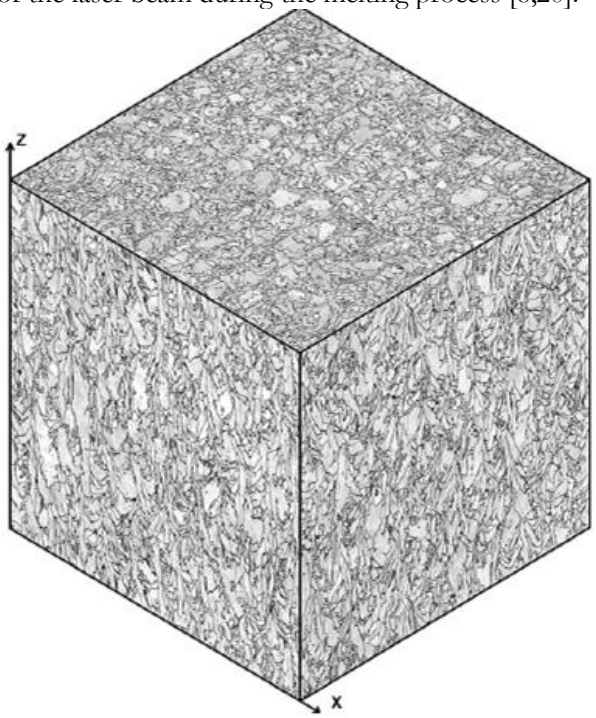

Fig. 8 *Directional Orientation of 3D-Printed EOS718 [10]*

The microstructure of Inconel 718 alloy produced by the SLM technique, observed after etching under an optical microscope, exhibits elongated grains with well-developed boundaries, whose arrangement corresponds to the solidification direction. The shape and size of the grains are highly heterogeneous, reflecting the uneven crystallization conditions during the additive manufacturing process. In some areas, a fine-grained matrix surrounding coarser grains is visible, resulting from repeated melting and recrystallization due to the overlap of laser tracks. The overall morphology corresponds to a lamellar and directionally oriented structure typical for SLM, which arises from high cooling rates, repeated thermal influence on underlying layers, and uneven solidification. During solidification, cooling occurs very rapidly, at rates of approximately 10^5–10^8 K/s in a small localized volume [20,21,22].

EDS analysis of EOS718 reveals an increased concentration of Nb and Mo in the areas analyzed, while the Cr content decreases. In cases of incomplete melting (Fig. 9) or the presence of defects in the powder bed (Fig. 10), microcracks and porosity may appear, often surrounded by oxide inclusions identified as Al_2O_3 or TiO_2[16,19].

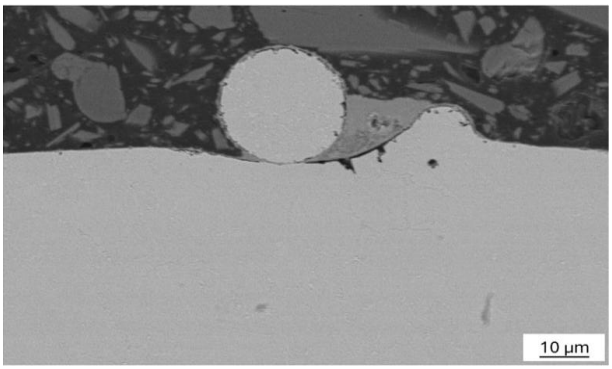

Fig. 9 *Unmelted powder particles*

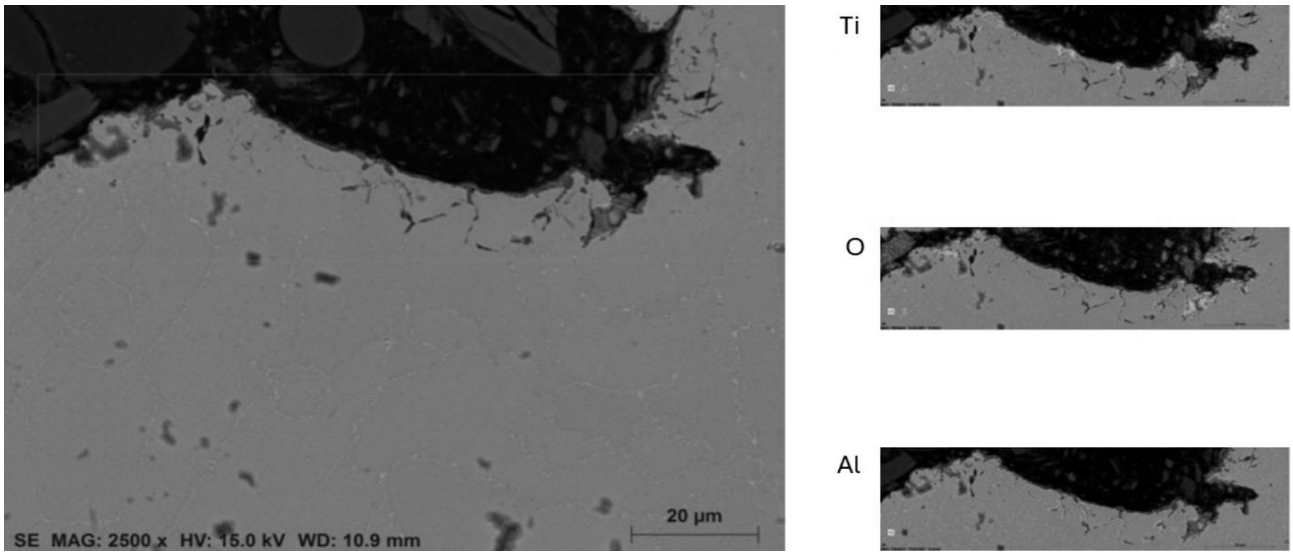

Fig. 10 *EDS map of oxide inclusions (specimen after exposure in air)*

After heat treatment, such as solution annealing followed by aging, the microstructure becomes homogenized, the Laves phase dissolves, and fine γ' and γ'' precipitates form. However, these phases cannot be distinguished by optical microscopy and appear only as slight contrast differences in SEM images. In BSE mode, the individual phases are clearly distinguishable – the γ matrix exhibits uniform contrast, while the δ phase at the grain boundaries appears brighter due to its higher Nb content (Fig. 11).

The Laves phase typically forms in interdendritic regions as bright, irregular features, while MC-type carbides, particularly NbC, appear as high-contrast dots or polygonal particles at the grain boundaries Fig. 12.

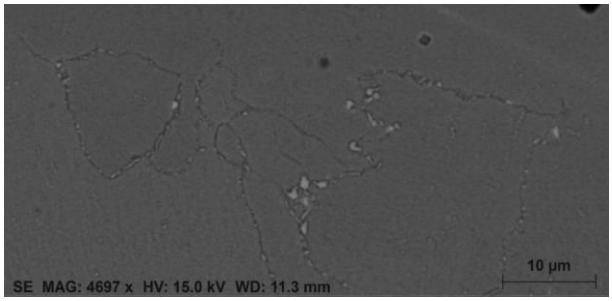

Fig. 11 *SEM image showing the γ and δ phase*

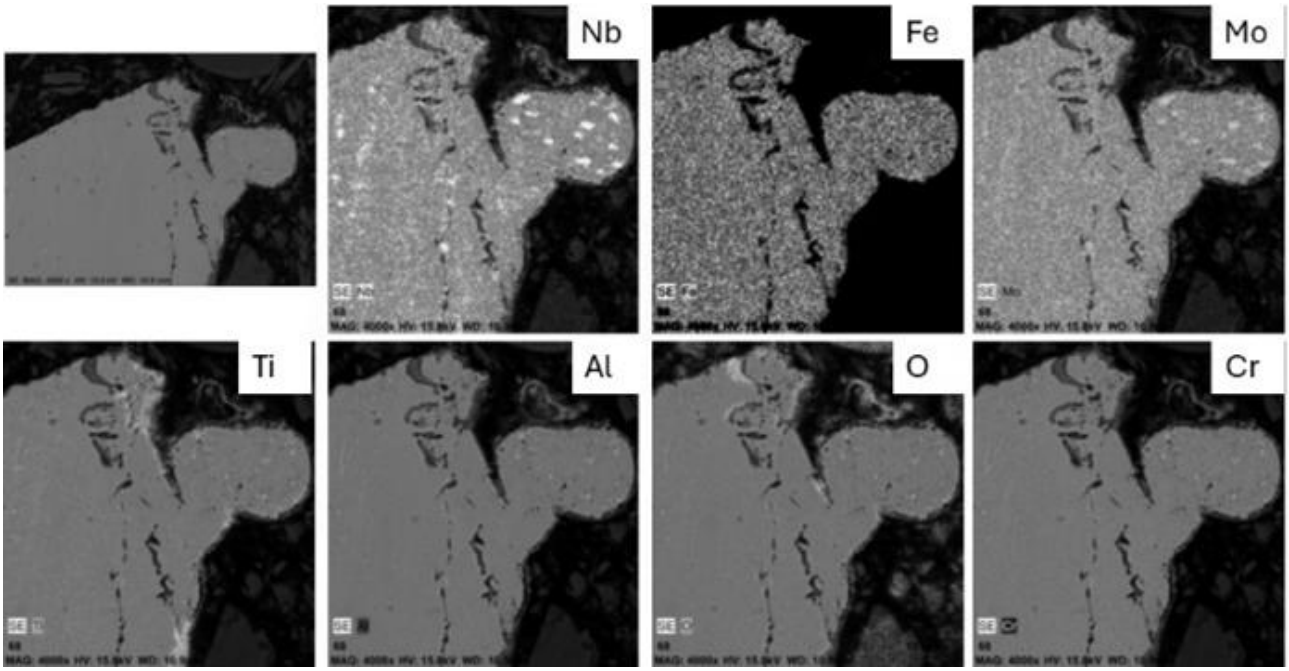

Fig. 12 *EDS EOS718*

Using EDS Fig. 13 the chemical composition of these phases can be characterized more precisely – the δ phase is rich in Nb and contains no Cr, MC carbides exhibit a high proportion of Nb and Ti with a low Cr content, and the Laves phase consists mainly of Nb and Mo with a smaller proportion of Fe and Cr [8,11,16,19,23,24,25].

Atomic %	O	Al	Ca	Ti	Cr	Fe	Ni	Nb	Mo
1	63.6	2.5	0.2	-	24.7	4.7	3.2	1.0	-
2	-	0.8	-	1.1	20.7	19.2	51.8	5.3	1.2
3	-	-	-	0.8	20.7	17.9	47.7	13.0	-
4	10.6	9.1	-	-	16.1	14.4	42.7	7.2	-
5	-	0.8	-	1.6	21.3	18.9	51.1	6.4	-
6	-	1.4	-	-	20.8	19.0	49.3	8.4	1.2
7	33.8	6.3	-	3.0	18.3	10.2	24.8	3.2	0.6
8	8.2	4.4	-		19.0	16.6	45.5	5.2	1.1

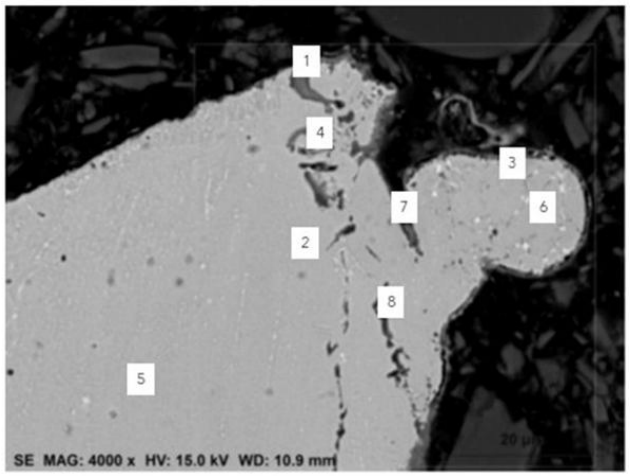

Fig. 13 *Chemical Composition – EDS Analysis (Specimen after Exposure)*

The microstructural evaluation in this study was primarily qualitative and aimed at a comparative investigation of the influence of the manufacturing route. Although the presence and distribution of individual phases (γ, δ, Laves, MC carbides) were clearly identified by SEM/EDS analysis, detailed quantitative phase fraction analysis and systematic oxide layer thickness measurements were not the primary objective. Such quantification would require a larger statistical dataset and advanced image analysis, which was beyond the scope of the present work. Nevertheless, the qualitative observations provided important insight into oxidation mechanisms.

3.3 Exposure in Model Environment

Studies [26,27,28] show that exposure of Inconel 718 alloy in air at 650 °C leads to oxide layer growth and microstructural changes. In conventionally processed material (Fig. 14) a predominantly compact Cr_2O_3 film forms, accompanied by localized Al-rich oxides at the grain boundaries. Recent studies confirm that oxides along the grain boundaries also contain Ti, and the oxidation depth increases with exposure time.

Microstructurally, this manifests as the growth of γ'/γ" precipitates and partial transformation of γ" → δ. In conventionally manufactured specimens, the oxide layer is more stable and protective due to the more homogeneous distribution of alloying elements. In contrast, additively manufactured specimens (Fig. 15), characterized by a fine-grained dendritic structure and higher Nb segregation, exhibit more intense intergranular oxidation, less continuous oxide layers, and consequently a higher susceptibility to degradation of mechanical properties.

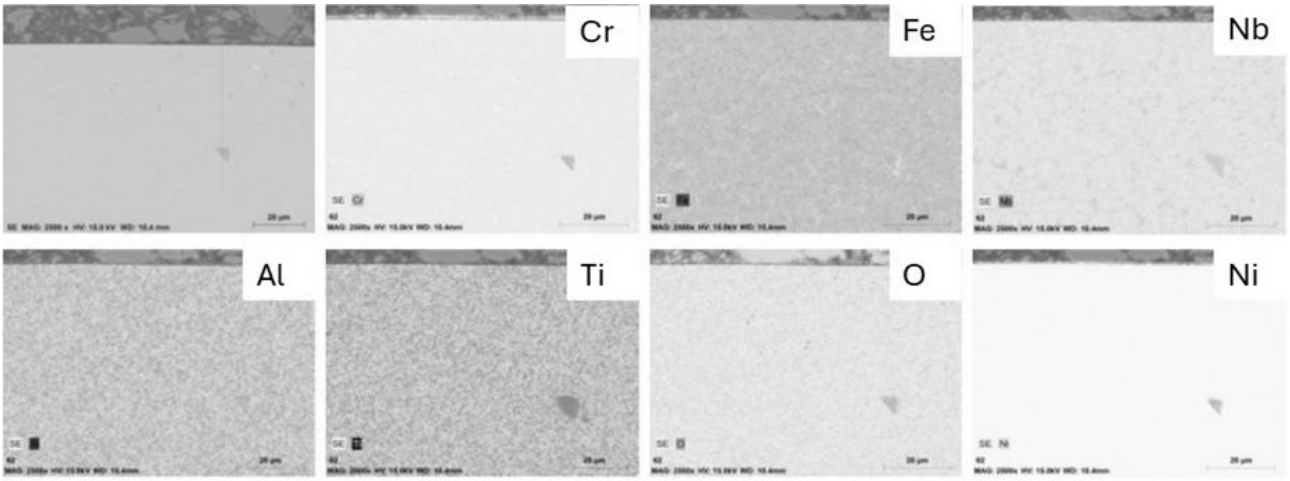

Fig. 14 *EDS map of the formed oxide layer on ALLOY718 after exposure in air – 650 °C, 1000 hours*

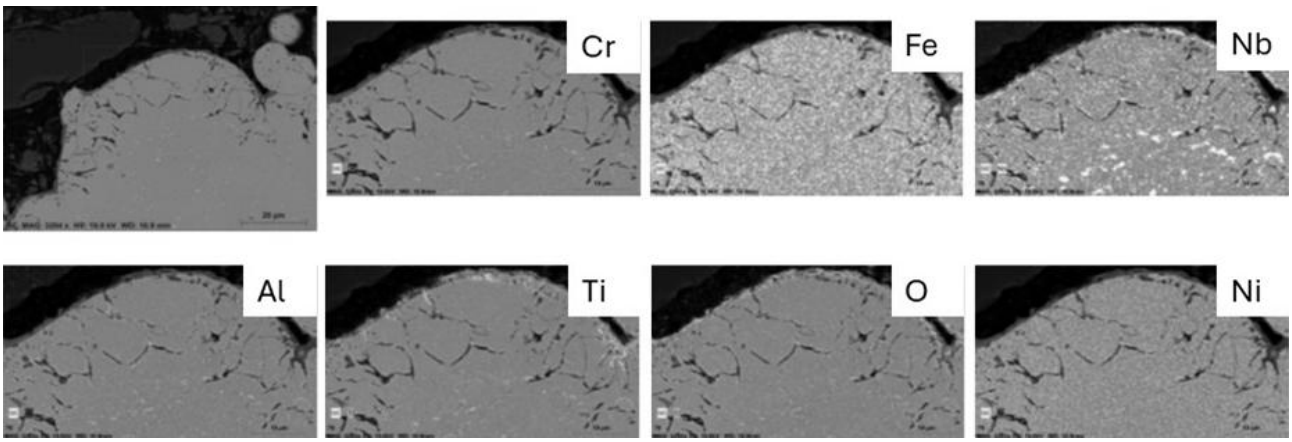

Fig. 15 *EDS map of the formed oxide layer on EOS718 after exposure in air - 650 °C, 1000 hours*

Based on available knowledge of Inconel 718 behavior in air and the general oxidation mechanisms of nickel-based superalloys in humid environments, it can be expected that water vapor accelerates oxidation due to enhanced oxygen diffusion, leading not only to surface layer growth but also to internal oxidation. Exposure of Inconel 718 alloy to steam at 650 °C results in significantly faster oxidation than in dry air, higher oxide mass accumulation, and intense intergranular oxidation. The outer oxide layer is primarily composed of Cr_2O_3, while Al-rich and Fe/Nb-rich oxides, as well as complex spinel phases, are frequently observed along grain boundaries (see Fig. 16).

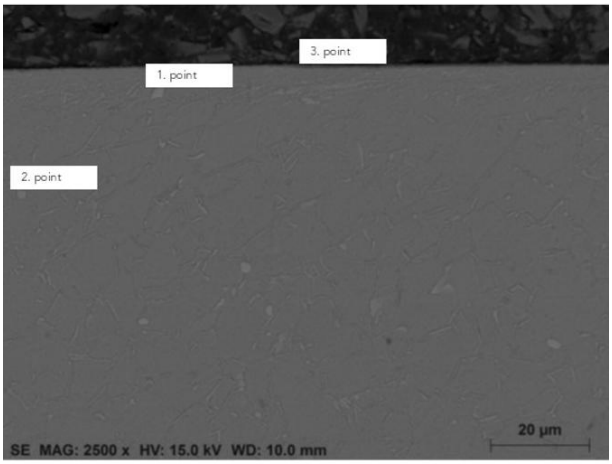

Atomic %	Al	Si	Ca	Ti	Cr	Fe	Ni	Nb	O
1	-	-	-	16.3	2.1	1.9	4.0	75.7	-
2	-	-	-	15.3	2.9	3.6	6.1	72.0	-
3	1.2	3.9	2.7	1.9	25.6	5.9	14.9	-	43.9

Fig. 16 *EDS analysis of the oxide layer on ALLOY718 – steam exposure*

Microstructurally, this is accompanied by coarsening of γ'/γ" precipitates and partial transformation of γ" → δ; Nb-rich segregated phases (Laves, MC carbides, δ), particularly present in additively manufactured specimens, promote deeper penetration of oxidation products (Fig. 17). Furthermore, water vapor destabilizes the passive layer, which is less continuous and less adherent, increasing susceptibility to intergranular degradation and reduc-ing the long-term mechanical resistance of the material [9,26,29].

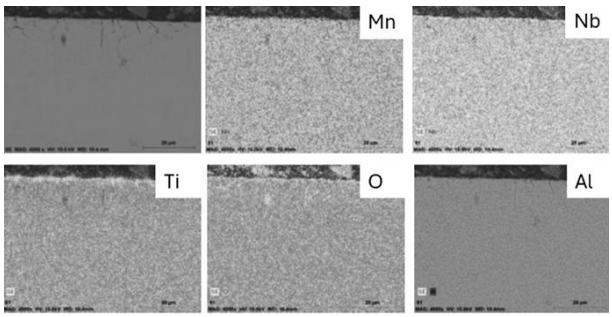

Fig. 17 *Elemental distribution map of the oxide layer on EOS718 - steam exposure*

Exposure in supercritical water (Fig. 18) has been investigated at various temperatures and pressures. Studies show the formation of an oxide layer primarily composed of spinel phases such as $Ni(Cr,Fe)_2O_4$ and $NiFe_2O_4$, with more complex structures forming at lower temperatures (425 °C), while higher temperatures (527.5–650 °C) lead to more uniform layering. Nb_2O_5 and Cr_2O_3 oxides were also identified. The presence of niobium, a significant alloying element, can negatively affect resistance to localized pitting corrosion, which was observed despite a low overall mass loss. Studies also indicate that oxidation follows a parabolic rate law, and higher iron content in the alloy promotes the formation of a more stable protective layer [4,30,31].

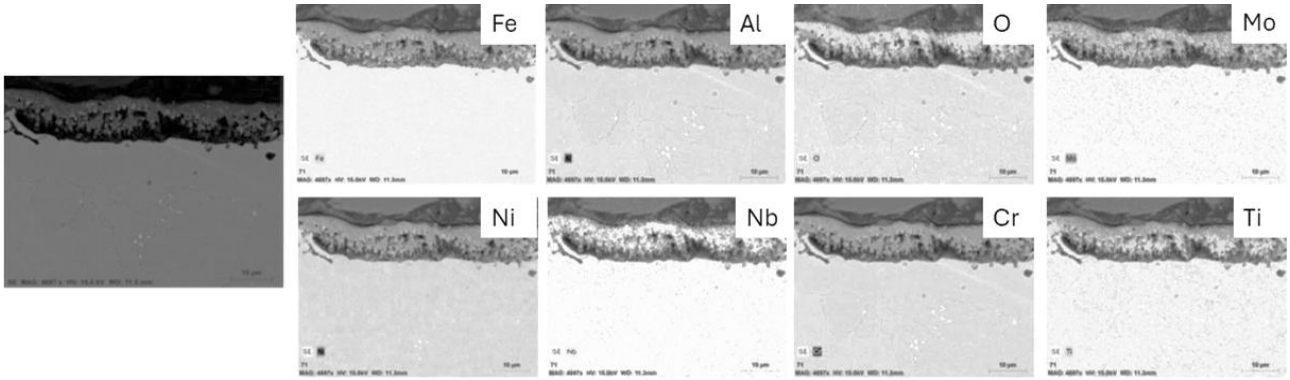

Fig. 18 *Elemental distribution map of EOS718 after exposure in SCW*

The corrosion mechanisms of nickel-based alloys in supercritical water can generally be explained by a combination of two dominant processes: growth of the barrier (inner) oxide layer via a solid-state mechanism and dissolution of the metallic matrix followed by oxide precipitation, leading to the formation of an outer layer. The dense, compact inner layer results from the solid-state growth mechanism, whereas the porous and less cohesive outer layer is a consequence of metal dissolution and oxide precipitation. The corrosion process itself occurs in two main stages. In the first stage, the metallic elements are oxidized, losing electrons and reacting with dissolved oxygen and supercritical water, forming oxides that deposit on the alloy surface. This step involves the transport of metal ions, such as Ni^{2+} and Fe^{3+}, into the surrounding SCW environment, while oxide ions (O^{2-}) migrate toward the inner interface of the oxide layer. In the second stage, the oxidation products either remain stable in the SCW environment or undergo further reactions until a thermodynamically stable oxide form is achieved.

Together, these mechanisms determine the resulting structure and protective properties of the formed oxide film [3,4,30,32,33]. Tab. 2 provides a comprehensive overview of the samples after exposure in all environments.

Tab. 2 *Summary of Oxide Layers Formed on Samples after Exposure in Different Environments*

	Before exposure	Exposure - air	Exposure - steam	Exposure - SCW
ALLOY718	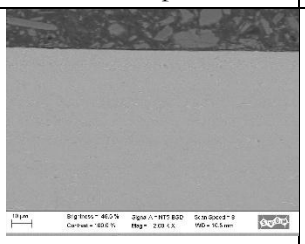	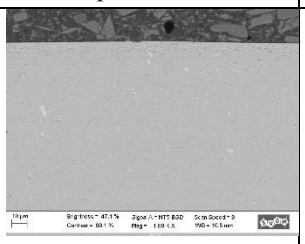	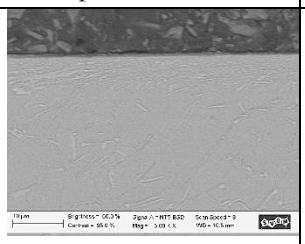	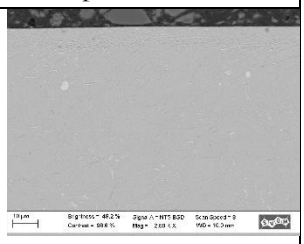
EOS718	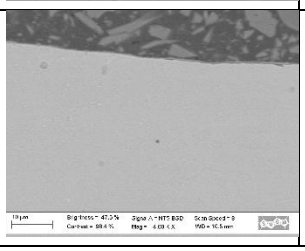	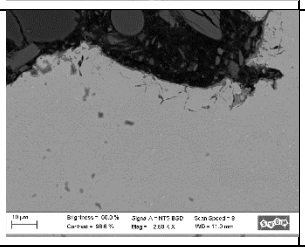	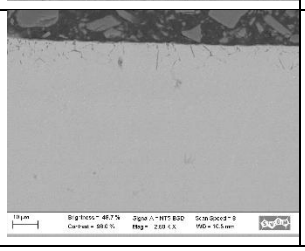	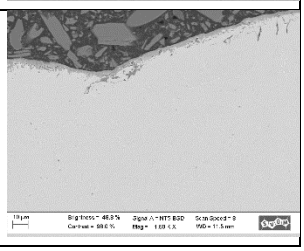

Although the oxide layers formed in the investigated environments are clearly visible in the presented SEM micrographs, their thickness was not quantitatively measured. As can be seen from the cross-sectional images throughout the manuscript, the oxide layers are generally very thin and, in several cases, discontinuous or locally non-uniform. The limited thickness of the oxide scale—often close to the resolution limit of conventional metallographic preparation—and its locally porous or non-compact character make reliable and statistically representative thickness measurements challenging. Any quantitative evaluation would require a significantly larger number of cross-sectional measurements combined with advanced image analysis or high-resolution techniques. Therefore, the present study focuses primarily on qualitative characterization of oxide morphology and elemental distribution, while systematic oxide layer thickness quantification was considered beyond the scope of this work.

The following graphs (Fig. 19) summarize all gravimetric data collected during the isothermal exposure of the materials at 650 °C for 100, 200, 500, and 1000 hours.

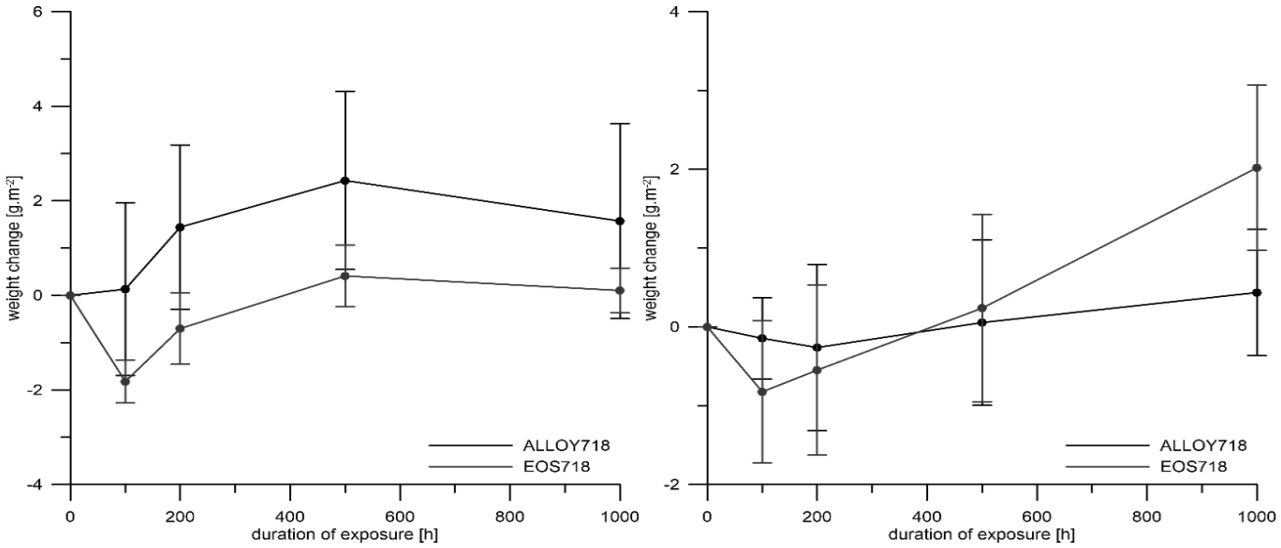

Fig. 19 *Graphs of mass losses/gains for exposure in air and steam*

Exposure in supercritical water was also carried out at 650 °C, but intermediate weighing of the samples was performed only after 500 and 1000 hours, as shown in Fig. 20. The corrosion process of nickel-based alloys in SCW can be divided into two stages. First, the metallic elements lose electrons and react with dissolved oxygen and supercritical water, forming oxides that grow on the alloy surface. This process

involves the transport of metal ions (e.g., Ni^{2+} and Fe^{3+}) into the SCW and the migration of O^{2-} ions into the inner oxide layer. In the second stage, the oxidation products either remain stable in the SCW or undergo further reactions until thermodynamically stable oxides are formed [3].

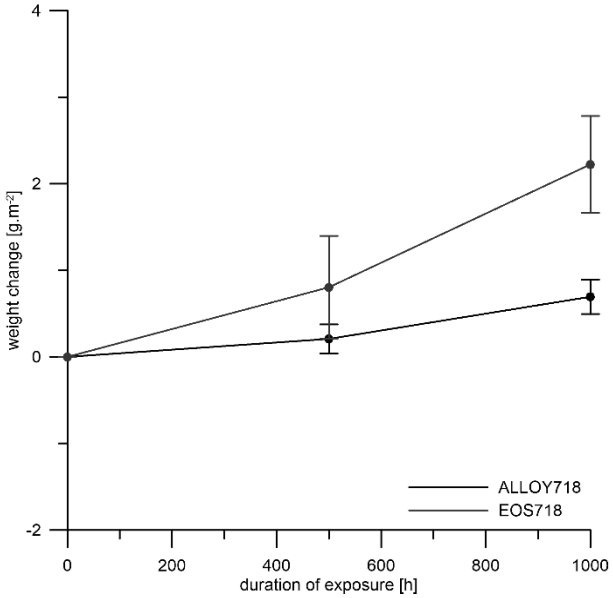

Fig. 20 *Graph of weight gains after exposure in SCW*

It should be noted that the measured mass changes were very small and, in several cases, close to the detection limit of the analytical balance. Therefore, the scatter in the experimental data must be interpreted with caution. Despite the small absolute mass changes, the observed trends were consistent across most specimens within each group, with the scatter reflecting both natural microstructural heterogeneity – particularly in additively manufactured samples – and the limited magnitude of measurable changes relative to the instrumental resolution. The gravimetric results indicate that the most pronounced mass changes occurred during the initial 200 hours of exposure, corresponding to the transient oxidation stage characterized by rapid formation of the primary oxide scale. After this period, the oxidation rate gradually decreased and approached a quasi-stationary regime. From a kinetic perspective, the behavior qualitatively follows parabolic-type kinetics typical for diffusion-controlled oxide growth in nickel-based superalloys. However, due to the low absolute mass gains and limited exposure duration, a rigorous determination of parabolic rate constants was not considered statistically robust and was therefore not performed. A comprehensive summary of the gravimetric data is presented in Fig. 21.

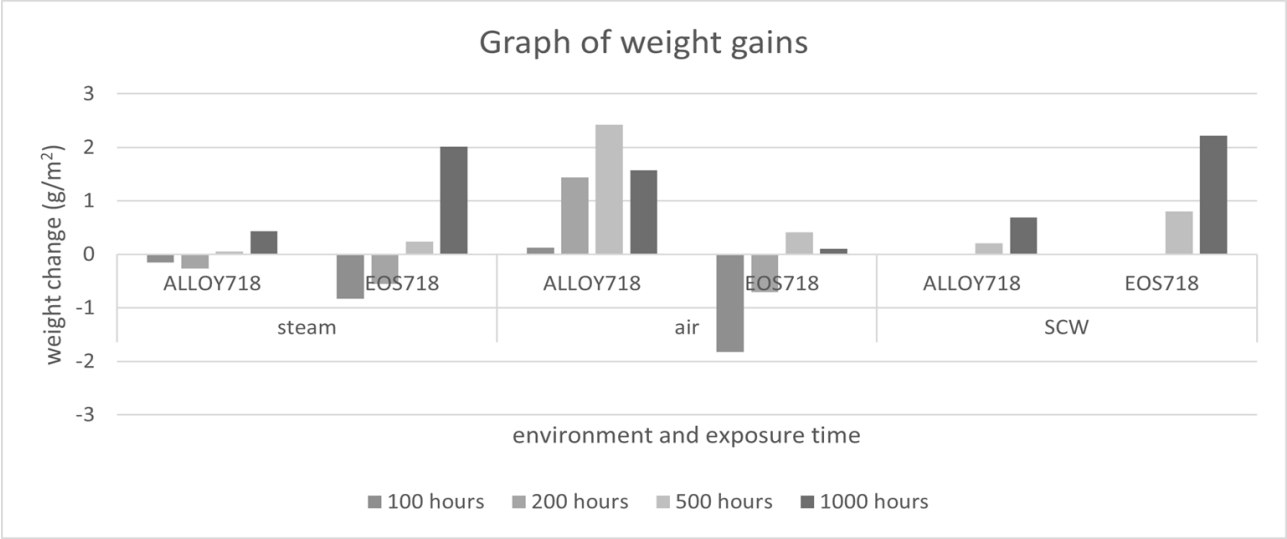

Fig. 21 *Graph of mass losses/gains*

Analysis of the mass loss and gain data shows that samples prepared by the SLM (Selective Laser Melting, i.e., 3D printing) method were the most susceptible to oxidation. This can be attributed to their microstructural characteristics, including a fine-grained dendritic structure with a high density of grain boundaries, segregated Nb-rich phases (Laves, δ, MC carbides), and microdefects, which promote more intense intergranular oxidation and deeper penetration of oxides into the material.

For both SLM and conventionally prepared samples, the most significant mass changes occurred during initial exposure period. Subsequently, oxidation gradually stabilized, and further changes were primarily mass gains due to the formation of a surface oxide layer. In the supercritical water (SCW) environment, only mass gains were measured for operational reasons. The most stable behavior, with minimal mass changes, was observed in conventionally prepared samples exposed to steam, consistent with their more homogeneous microstructure and continuous, compact surface oxide layer.

4 Conclusions

In this study, Inconel 718 alloys prepared by two manufacturing methods—conventional processing (ALLOY718) and additive manufacturing using SLM (EOS718, 3D printing)—were monitored and compared during exposure in three environments: air, steam, and supercritical water (SCW). Gravimetric changes in sample mass were recorded, and the formation and characteristics of the oxide layer were observed.

The results indicate that the manufacturing route significantly influences oxidation behavior. Additively manufactured samples exhibited higher susceptibility to oxidation, which can be attributed to their fine dendritic microstructure, higher density of grain boundaries, segregation of Nb-rich phases (Laves and δ), and microstructural heterogeneities inherent to the SLM process. These features promote localized and intergranular oxidation and affect oxide scale development

The most pronounced mass changes occurred during the initial 200 hours of exposure, corresponding to a transient oxidation stage with rapid formation of the primary oxide scale. During this period, mass losses were primarily associated with the volatilization of specific alloying elements, particularly chromium and molybdenum. Chromium typically forms a stable Cr_2O_3 layer; however, at elevated temperatures and in the presence of steam, part of the oxide may sublimate, while volatile oxides of other elements can disperse into the environment. In SCW, no mass loss was observed due to the timing of the initial weighing. Subsequently, all samples exhibited minor mass gains, although overall changes were very small and often near the detection limit of the analytical balance. Even after 1000 hours of exposure, mass gains were typically only a few grams per square meter, corresponding to a negligible corrosion rate (~0.0025 mm/year).

From a kinetic perspective, oxidation qualitatively followed parabolic-type behavior typical for diffusion-controlled oxide growth in nickel-based superalloys. However, due to the very low absolute mass changes and limited exposure duration, quantitative determination of oxidation rates or parabolic rate constants was not statistically robust and was therefore not performed.

Given the small magnitude of mass changes and their proximity to measurement limits, conclusions should be interpreted primarily in terms of qualitative trends rather than precise quantitative corrosion rates. For more accurate kinetic evaluation and a more robust statistical analysis, longer exposure times and complementary high-resolution characterization techniques would be beneficial in future studies.

Acknowledgement

This result was created within the project TN02000018 "National Centre of Competence ENGINEERING", which is co-financed from the state budget by the Technology Agency of the Czech Republic under the National Centres of Competence Programme.

References

[1] KHAN, H. I. ZHANG, N., ZHU, Z., JIANG, D., ASIF, T., XU, H. (2018). Behavior and susceptibility to stress corrosion cracking of a nickel-based alloy in superheated steam and supercritical water. In: *Materials and Corrosion*. 1-9. DOI: https://doi.org/10.1002/maco.201810237

[2] ZHANG, Q., TANG, R., LI, C., LUO, X., LONG, CH., YIN, K. (2009). Corrosion Behavior of Ni-base alloys in supercritical water. In: *Nuclear Engineering and Technology*. 41 (1). DOI:10.5516/NET.2009.41.1.107

[3] GUO, S., XU, D., LI, Y., GUO, Y., WANG, S., MACDONALD, D. D. (2021). Corrosion characteristics and mechanisms of typical Ni-based corrosion-resistant alloys in sub-and supercritical water. In: *The Journal of Supercritical Fluids*. Vol. 170. DOI: https://doi.org/10.1016/j.supflu.2020.105138

[4] SUN, CH., HUI, R., QU, W., YICK, S. (2009) Progress in corrosion resistant materials for supercritical water reactors. In: *Corrosion Science*. Vol. 51. pp. 2508-2523. DOI: https://doi.org/10.1016/j.corsci.2009.07.007

[5] LIU, W., ZHAO, L., GONG, B., TANG, R., CHEN, H. (2025). Corrosion behavior and slow strain rate tensile testing of Inconel 718 alloy in deaerated supercritical water at 650 °C. In: *Journal of Materials Research and Technology,* Vol. 35, pp. 5945–5955. ISSN 2238-7854, DOI: https://doi.org/10.1016/j.jmrt.2025.02.254.

[6] FOURNIER, L., BOSCH, C., DELAFOSSE, D. (2001) Stress Corrosion of Nickel Base Superalloys in Aerated Supercritical Water. Paper presented at the CORROSION 2001, Huston, Texas, March 2001, paper number: NACE-01361.

[7] CHEN, Y., ZHANG, K., HUANG, J., HOSSEINI, S. R. E., LI, Z. (2016). Characterization of heat affected zone liquation cracking in laser additive manufacturing of Inconel 718. In: *Materials and Design,* Vol. 90, pp. 586-594. DOI:

http://dx.doi.org/10.1016/j.matdes.2015.10.155

[8] HOSSEINI, E., POPOVICH, V. A. A review of mechanical properties of additively manufactured Inconel 718. (2019). In: *Additive Manufacturing*. Vol. 30. DOI: https://doi.org/10.1016/j.addma.2019.100877

[9] MADHUSUDAN, S., EPIFANO, E. FAVERGEON, J., SANVIEMVONGSAK, T., MARÉCHAL, D., MONCEAU, D. High Temperature Intergranular Oxidation of Nickel Based Superalloy Inconel 718. (2024). In: *High Temperature Corrosion of Materials*. Vol. 101. pp. 873-884. DOI: https://doi.org/10.1007/s11085-024-10260-z

[10] POLOCH, A. Hodnocení mechanických vlastností niklové superslitiny Inconel 718 připravené pokročilou technologii DMLS. Studentská tvůrčí činnost 2019. České vysoké učení technické v Praze. Fakulta strojní. (dostupné online: https://stc.fs.cvut.cz/pdf19/9515.pdf) [citované: 22.09.2025].

[11] Nickel Alloy, Corrosion and Heat Resistant, Bars, Forgings, and Rings 52.5Ni - 19Cr - 3.0Mo - 5.1Cb (Nb) - 0.90Ti - 0.50Al - 18Fe Consumable Electrode or Vacuum Induction Melted 1950 °F (1066 °C) Solution Heat Treated, Precipitation Hardenable: AMS5664F. 7. SAE International, 2017

[12] ČERNÝ, I., KEC, J., POLOCH, A., ZETEK, M. Mechanical properties and high-cycle fatigue strength of 3D printed Inconel 718 alloy and effects of high-temperature exposure to corrosive atmosphere. *AIP Conference Proceedings 2309*, 020026 (2020). DOI: https://doi.org/10.1063/5.0035400.

[13] ASGHAR. K, NGULIMI, M. F., KIM, S., SEO, B. K, ROH, CH. (2024). Cobalt recovery from industrial and nuclear waste resources: A review. In: *Chemical Engineering Journal Advances*. Vol. 20. ISSN: 2666-8211, DOI: https://doi.org/10.1016/j.ceja.2024.100668

[14] FRANCO-CORREA, J. C., MARTÍNEZ-FRANCO, E., ALVARADO-OROZCO, J. M., et al. (2021). Effect Of Conventional Heat Treatments on the Microstructure and Microhardness of IN718 Obtained by Wrought and Additive manufacturing. In: *Journal of Materials Engineering and Performance*. Vol.30, pp. 7035-7045. DOI: https://doi.org/10.1007/s11665-021-06138-9.

[15] CHAMANFAR, A., SARRAT, L., JAHAZI, M., ASADI, M., WECK, A., KOUL, A. K. Microstructural characteristics of forged and heat treated Inconel-718 disks. (2013). In: *Materials and Design*. Vol. 52. pp. 791-800. DOI: https://doi.org/10.1016/j.matdes.2013.06.004

[16] GHAEMIFAR, S., MIRZADEH, H. Precipitation kinetics of niobium carbide (NbC) during homogenization heat treatment of additively manufactured Inconel 718 superalloy. (2023). In: *Journal of materials research and technology*. Vol 25. pp. 1774-1781. DOI: https://doi.org/10.1016/j.jmrt.2023.06.069

[17] SMITH, W. Structure and properties of engineering alloys. New York: McGraw-Hill. (1981). ISBN 00-705-8560-1.

[18] POPOVICH, V. A., BORISOV, E. V., POPOVICH, A. A., SUFIIAROV, V. Sh., MASAYLO, D. V., ALZINA, L. Functionally graded Inconel 718 processed by additive manufacturing: Crystallographic texture, anisotropy of microstructure and mechanical properties. (2016). In: *Materials and Design*. DOI: https://doi.org/10.1016/j.matdes.2016.10.075

[19] STEVENS, E. L., TOMAN, J., To, A. C., CHMIELUS, M. Variation of hardness, microstructure, and Laves phase distribution in direct laser deposited alloy 718 cuboids. (2017). In: *Materials and Design*. Vol. 119, pp. 188-198. DOI: https://doi.org/10.1016/j.matdes.2017.01.031

[20] ADOMAKO, N. K., HAGHDADI, N., PRIMIG, S. Electron and laser-based additive manufacturing of Ni-based superalloys: A review of heterogeneities in microstructure and mechanical properties. (2022). In: *Materials and Design*. Vol. 223. DOI: https://doi.org/10.1016/j.matdes.2022.111245.

[21] DEBROY. T., WEI, H. L., ZUBACK, J. S., MUKHERJEE, T., ELMER, J. W., MILEWSKI, J. O., BEESE, A. M., WILSON-HEID, A., DE, A., ZHANG, W. Additive manufacturing of metallic components – Process, structure and properties. (2018). In: *Progress in Materials Science*. Vol. 92, pp. 112-224. DOI: https://doi.org/10.1016/j.pmatsci.2017.10.001.

[22] MUKHERJEE, T., MANVATKAR, V., DE, A., DEBROY, T. Dimensionless numbers in additive manufacturing. (2017). In: *Journal of Applied Physics*. Vol. 121 (6). DOI: https://doi.org/10.1063/1.4976006.

[23] LAKSHMI L. PARIMI, RAVI. G. A., CLARK, D., ATTALLAH, M. M. Microstructural and texture development in direct laser fabricated IN718. (2014). In: *Materials Characterization*. Vol. 89. pp. 102-111. DOI: https://doi.org/10.1016/j.matchar.2013.12.012.

[24] JIA. Q., GU. D. Selective laser melting additive manufacturing of Inconel 718 superalloy parts: Densification, microstructure and properties. (2014). In: *Journal of Alloys and Compounds*. Vol. 585. pp. 713-721. DOI: https://doi.org/10.1016/j.jallcom.2013.09.171.

[25] LIU, F., LYU, F., LIU, F., LIN, X., HUANG, CH. Laves phase control of Inconel 718 superalloy fabricated by laser direct energy deposition via δ aging and solution treatment. (2020). In: *Journal of Materials Research and Technology*. Vol. 9 (5), pp. 9753-9765. DOI: https://doi.org/10.1016/j.jmrt.2020.06.061.

[26] GARAT, V., DELEUME, J., CLOUE, J. M., ANDRIEU, E. High Temperature Intergranular Oxidation of Alloy 718. In: *Proceedings of the Symposium on Superalloys 718, 625, 706 and Derivatives*. Pittsburgh, PA, USA. 2-5 October 2005. pp. 559-569. ISBN 978-0-87339-602-8.

[27] BEYHAGHI, M., ROUHANI, M., HOBLEY, J., JENG, Y.-R. In-situ and ex-situ comparsion of oxidation of Inconel 718 manufactured by selective laser melting and conventional methods up to 650 °C. (2021). In: *Applied Surface Science*. Vol. 569. DOI: https://doi.org/10.1016/j.apsusc.2021.151037.

[28] QIN, L., REN, P., YI, Y., CHEN, D., LU, Y., SUN, D., SHI, CH., ZHOU, S. Microstructure, high-temperature cyclic oxidation, and hot corrosion behaviors of Inconel 718 alloy produced by laser-induction hybrid cladding. (2024). In: *Journals of Materials Research and Technology*. Vol. 32. pp. 550-564. DOI: https://doi.org/10.1016/j.jmrt.2024.07.200.

[29] CHEN, H., WANG, H., SUN, Q., LONG, CH., WEI, T., KIM, S. H., CHEN, J., KIM, CH., JANG, CH. Oxidation behavior of Fe-20Cr-25Ni-Nb austenitic stainless steel in high-temperature environment with small amount of water vapor. (2018). Vol. 145. pp. 90-99. In: *Corrosion Science*. DOI: https://doi.org/10.1016/j.corsci.2018.09.016

[30] RODRIGUEZ, D., MERWIN, A., ZACHARY, K., CHIDAMBARAM, D. (2017). Surface chemistry and corrosion behavior of Inconel 625 and 718 in subcritical, supercritical, and ultrasupercritical water. In: *Applied Surface Science*, Vol. 404, pp. 443 - 451. ISSN 0169-4332, DOI: https://doi.org/10.1016/j.apsusc.2017.01.119

[31] MA S., LUO, Y., ZHANG, O., WANG, H., QIU, S. (2014). Study on Corrosion Behavior of Candidate Materials in 650 °C Supercritical Water. In: *Atomic Energy Science and Technology*, Vol. 48 (3), pp. 416-421. ISSN 1000-6931, DOI: 10.7538/yzk.2014.48.03.0416

[32] CHEN, Y., SRIDHARAN, K., ALLEN, T. (2006). Corrosion behavior of ferritic-martensitic steel T91 in supercritical water. In: *Corrosion Science,* Vol. 48(9), pp. 2843-2854. DOI: https://doi.org/10.1016/j.corsci.2005.08.021

[33] HUANG, T., SU, H., ZHAOU, Y., WANG, J., ZHANG, L., CHEN, K. Comparison of the corrosion behavior of four Fe-Cr-Ni austenitic alloys in supercritical water. (2025). In: *Journal of Nuclear Materials*. Vol. 603. DOI: https://doi.org/10.1016/j.jnucmat.2024.155409.